Supplementary Information for:

Strong Plasmon-enhancement of the Saturation Photon Count Rate of Single Molecules

Yuyang Wang,[†,‡] Matĕj Horáček,[†,‡] and Peter Zijlstra[*,†,‡]

†*Department of Applied Physics, Eindhoven University of Technology, Eindhoven, The Netherlands*

‡*Institute for Complex Molecular Systems, Eindhoven, The Netherlands*

E-mail: p.zijlstra@tue.nl

Contents

Sample preparation

Glass coverslips ($22 \times 40mm^2$, thickness #1.5) were purchased from Menzel Gläser and were first sonicated for 15 min in methanol and subsequently functionalized with a thiolated silane by immersion in 5% (3-Mercaptopropyl)trimethoxysilane (MPTMS, Sigma-Aldrich) in ethanol for 15 minutes.

AuNRs purchased from Nanoseedz (NR-25-650) were redispersed in a 1 mM cetyltrimethylammonium bromide (CTAB) aqueous solution with an OD of 2, and spin-coated on thiolated coverslips. The coverslips with immoblized AuNRs were flushed with distilled water and phosphate buffer saline (PBS) to remove excess CTAB. These procedures result in deposited AuNRs with a density of $\sim 3\mu m^{-2}$.

All oligos were purchased from IDT Ltd., and purified by HPLC. The sequences are shown in Table 1. Docking strands are conjugated to the immobilized bare AuNRs in citrate buffer (100 mM, pH 3, 1 M NaCl). 78 µL of the citrate buffer, 2 µL of 50 µM stock solution of docking strands, 10 µL of 50 µM stock solution of antifouling strands, and 10 µL of 1000 mM Tris(2-carboxyethyl)phosphine hydrochloride (TCEP, Sigma-Aldrich: C4706) aqueous solution is added to an eppendorf tube and mixed with a vortexer, forming a docking solution ready for functionalization. The docking solution is left on the bench for 30 min to allow TECP to cleave dithiols in the solution. The high ionic strength in the citrate buffer and low pH reduces electrostatic repulsion between the ssDNA docking strands and the AuNR surface and between neighboring docking sites. Then the docking solution is dropcast on the coverslip with immobilized AuNRs for at least 1 h and rinsed with distilled water and PBS. To prevent drying the sample is then immediately mounted in a flow cell (Warner instrument) for single-molecule fluorescence measurements. A solution of fluorescently labeled imager strands was prepared freshly before microscope experiments, and was diluted to the desired concentration using PBS buffer (137 mM, pH 7.4, 500 mM NaCl).

We estimated the spacing between the fluorophore and the particle by adopting the ideal chain model. This has been shown to be a good approximation for DNA in high ionic strength

solutions.[1,2] Herein the time-averaged end-to-end distance of a polymer chain is given by $\sqrt{<\vec{R}^2>} = \sqrt{N}l$, where N is the number of polymer segments and l is the monomer length. We assumed that the monomer length of single stranded DNA $l_{\mathrm{ss}} = 0.50$nm, and of double stranded DNA $l_{\mathrm{ds}} = 0.34$nm.[2] The time-averaged end-to-end distance for the 30 nt docking strand with a 9 nt complementary double helix holding the fluorophore is then $R^{30nt}_{\mathrm{far\text{-}end}} \simeq 4$nm, where we have added 1 nm to account for the C6 linkers in the functionalized DNA strands. For the 15 nt docking strand with an inverted 9 nt complementary double helix we find $R^{15nt}_{\mathrm{near\text{-}end}} \simeq 1.5$nm.

Table 1: DNA sequences[a]

Strand names (length)	5' mod	Sequence	3' mod
Docking strand (30 nt)	thiol	CTA CTT CAT ACG CTT CCA CTA ATA CAT CTA	
Docking strand (15 nt)	thiol	CCA CTA ATA CAT CTA	
Imager strand (far-end)	ATTO647N	T TAG ATG TAT	
Imager strand (near-end)		TAG ATG TAT C	ATTO647N

[a] Complementary parts are marked in red.

Single-molecule fluorescence microscopy and single-particle spectroscopy

Single-fluorescence microscopy was performed using a Nikon Ti-E inverted microscope configured for a custom built total internal reflection fluoresence (TIRF) imaging. The flow cell containing immobilized DNA-functionalized AuNRs is mounted in the microscope. The use of a flow cell facilitates the constant flow of imager solution and refreshes the transient binding to docking strands of new single imagers. The flow is controlled at a rate of $100\,\mu\mathrm{Lmin}-1$. The sample is excited with $637\,\mathrm{nm}$ CW laser light (solid-state laser, Coherent OBIS) through an oil immersion TIRF objective (1.49 NA APO TIRF 60×, Nikon). The Perfect Focus System (PFS, Nikon) was kept on during the fluorescence measurement. Fluorescence emission is directed to an Andor iXon 888 EMCCD camera through a $650\,\mathrm{nm}$ long

pass dichroic mirror (Thorlabs) and a 640/670 nm band-pass filter pair (Thorlabs). An EM Gain of 100, and an integration time of 100 ms was used for the detection of single-molecule fluorescence. Camera counts were converted to photon counts under the photon counting mode of the EMCCD camera , and a conversion factor, that is camera counts divided by photon counts, of 0.05 was found. A region of interest of 300×300 px or 40×40 µm^2 was captured during imager binding. 5 - 10 min videos were taken to collect fluorescence bursts on single AuNRs due to imager binding events.

Calibration of TIRF excitation power density

The power density (I_{exc}, [W m^2]) of the excitation laser in the evanescent field was calibrated by converting the incident power (I_{inc}, [W]) measured by a power meter directly at the exit of the objective. I_{inc} is then converted to I_{exc} according to $I_{\mathrm{exc}} = \eta_{\mathrm{TIR}} I_{\mathrm{inc}} / A$, where η_{TIR} is the field enhancement factor in the evanescent field and A the size of illuminated area of the excitation beam. η_{TIR} takes into account the increase of the average intensity close to the water-glass interface, and depends on the refractive indices of the media ($n_{\mathrm{water}}, n_{\mathrm{glass}}$) and on the angle of incidence (θ).[3] In our calculation we use $\eta_{\mathrm{TIR}} = 2$ based on a calculation with $n_{\mathrm{water}} = 1.33, n_{\mathrm{glass}} = 1.52$, and $\theta \simeq 70^o$. A was measured by fitting the TIR-illuminated background with a Gaussian function and calculated to the area of a circle with a diameter that equals the full-width-half-maximum (FWHM) of the fitted Gaussian. Measurements presented here were performed for $I_{\mathrm{exc}} = 5.2 \times 10^5 - 2.6 \times 10^7$ W m^{-2} corresponding to I_{inc} of 0.002 - 0.110 W.

Saturation of single molecules without antenna

The saturation curve of non-enhanced imagers was measured by flushing the imager strand into a clean flow cell containing no nanoparticles. The random sticking of single imagers was captured by the EMCCD as diffraction limited spots. The diffraction limited spots were

then fitted with 2D-Gaussian functions, and the PCR was calculated as the volume under the fitted Gaussian after conversion from camera counts to photon counts. We filtered out sticking events that lasted shorter than 2 frames to exclude bias due to photo-bleaching. The saturation curve and fitted free space PCR_{max}^0 and I_{sat} were found to be comparable with those in an solution-phase ensemble control measurement. In Figure S1 we show the PCR distributions and free-space saturation curve of single ATTO 647N molecules coupled to imager DNA strands.
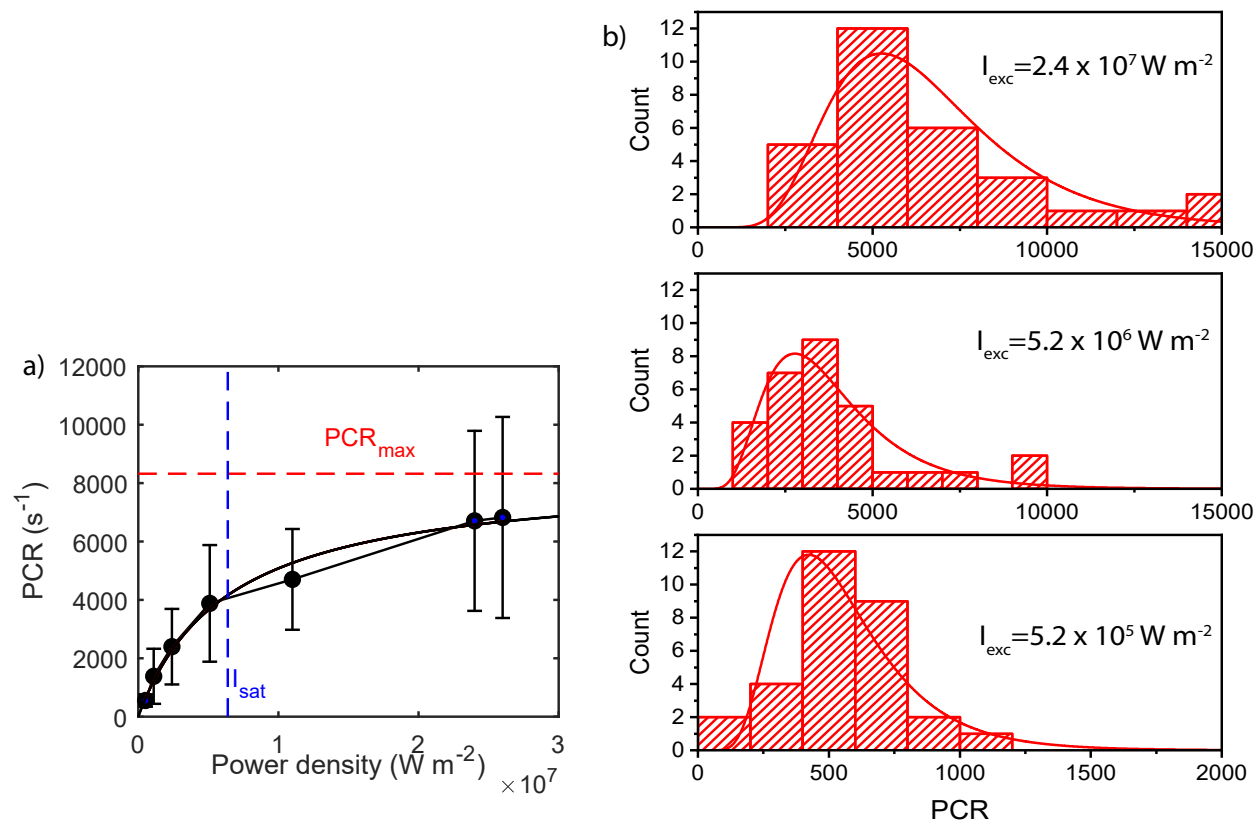

Figure S 1: (a) Saturation curve of single non-enhanced ATTO647N imagers. (b) Histograms of PCR distributions of non-enhanced single ATTO647N imagers under different excitation power densities.

Fluorescence timetraces as a function of power density and SPR wavelength

The effect of photobleaching is negligible due to the refreshment of fluorophores by repeated DNA hybridization, and is further evidenced by the fact that the duration of the fluorescence bursts is independent of laser power density. In Figure S2 we show the time traces and bright times t_{bright} as a function of power densities. We show here t_{bright} is independent of power density, exhibiting mean values ~ 0.4 s which matches previous results for the same DNA sequence.[4] In Figure S3 we show the fluorescence time traces collected three different single gold nanorod with different SPR wavelengths. No dependence of t_{bright} was found on SPR wavelength either.
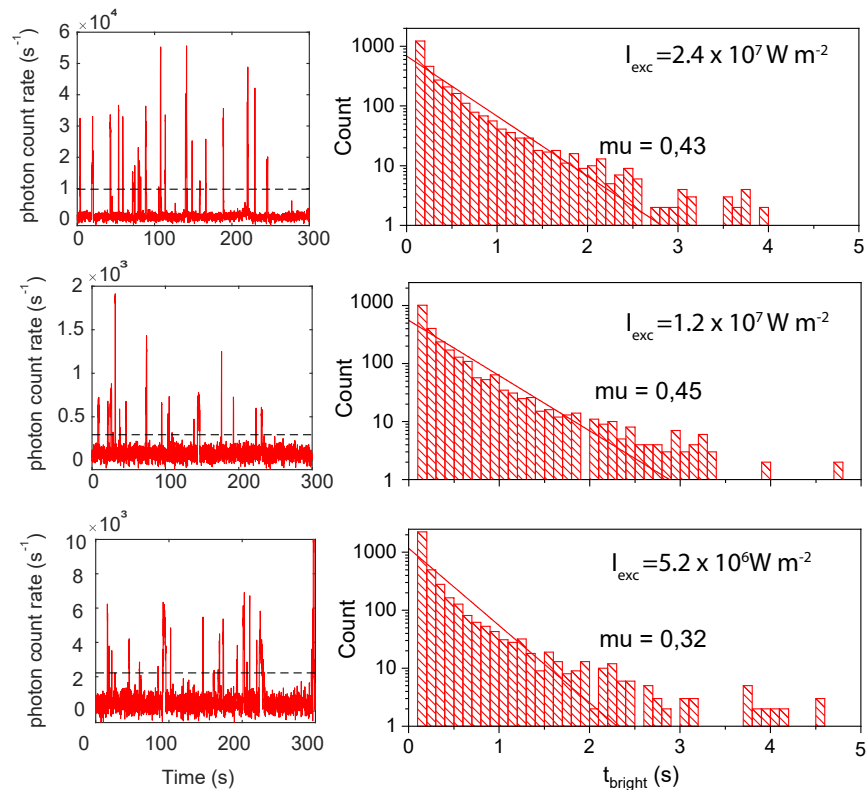

Figure S 2: Fluorescence timetraces from the same single nanorod and corresponding t_{bright} detected at decreasing power densities. For better statistics, t_{bright} from thousands of binding events collected from multiple nanorods are plotted in the histogram for measurement under different power densities.
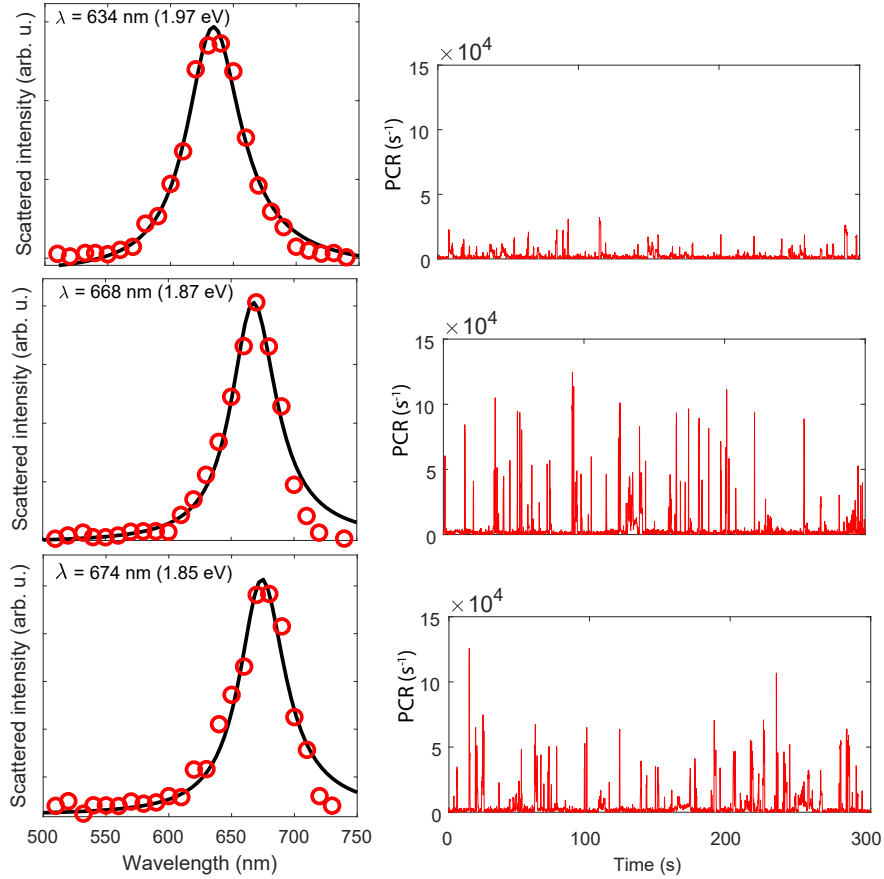
Figure S 3: Fluorescence timetraces from single nanorod with different SPR wavelengths coming from the same dataset as in Figure S2 Left panel: single particle spectra measured from hyperspectral spectroscopy. Red dots are measured scattering intensities and black lines the respective Lorenztian fittings. SPR wavelength λ of 634, 668 and 674 nm are found for three nanorods. Right panel: timetraces from corresponding nanorods measured under $I_{\mathrm{exc}} = 2.4 \times 10^7 \mathrm{W\,m}^{-2}$. Integration time $t_{\mathrm{int}} = 100ms$.

Derivation of single molecule photon count rate

The expression of the single-molecule PCR including saturation is derived here.[5,6] When a molecule is illuminated, a fraction of light proportional to its absorption cross-section σ_{abs} is absorbed leading to excitation of the molecule. The rate of absorption γ_{abs} in photons per second, is given by:

$$\gamma_{\text{abs}} = \frac{\sigma_{\text{abs}} I_{\text{exc}}}{h\nu}, \tag{1}$$

where I_{exc} is the incident excitation intensity (W m^{-2}), h is Planck's constant, and ν is the frequency of the incident light. Upon absorption of a photon the molecule is excited to the excited state S_1. Decay from the excited state can occur via either radiative decay (fluorescence), non-radiative decay, or intersystem crossing, with corresponding rates of γ_{r}, γ_{nr}, and γ_{isc} respectively. This yields the total decay rate $\gamma_{\text{tot}} = \gamma_{\text{r}} + \gamma_{\text{nr}} + \gamma_{isc}$ and a fluorescence lifetime $\tau_{\text{lifetime}} = \frac{1}{\gamma_{\text{tot}}}$. Saturation can occur when the rate of absorption γ_{abs} approaches the total decay rate γ_{tot}. The illumination intensity at which saturation occurs, I_{sat} (W m^{-2}) is defined as:

$$I_{\text{sat}} = \frac{\gamma_{\text{tot}} h\nu}{\sigma_{\text{abs}}}. \tag{2}$$

When the molecule is in the excited state it cannot absorb another photon for an average time of τ_{lifetime}. Once the molecule has relaxed to its ground state it becomes receptive to excitation again but has to wait for an average time of τ_{abs} (given by $\tau_{\text{abs}} = \frac{1}{\gamma_{\text{abs}}}$). This results in a reduced probability P_{a} for photon absorption, which can be written as:

$$P_{\text{a}} \propto \frac{\tau_{\text{abs}}}{\tau_{\text{lifetime}} + \tau_{\text{abs}}}, \tag{3}$$

assuming that the photons arrive at random over the time interval of $\tau_{\text{lifetime}} + \tau_{\text{abs}}$. Combining above equations yields:

$$P_{\text{a}} \propto \frac{I_{\text{sat}}}{I_{\text{exc}} + I_{\text{sat}}}. \tag{4}$$

Combined with the setup's collection efficience η_{col}, the absorption cross section σ_{abs}, and the fluorescence quantum yield $\phi = \gamma_{\text{r}}/\gamma_{\text{tot}}$, we write the emitted photon count rate (PCR) of a molecule as:

$$PCR = \eta_{\text{col}} \frac{\sigma_{\text{abs}}}{h\nu} \phi \frac{I_{\text{exc}} I_{\text{sat}}}{I_{\text{exc}} + I_{\text{sat}}}. \tag{5}$$

Numerical simulations

Numerical simulation of the fluorescence enhancement was performed using a boundary element method (BEM) using the MNPBEM toolbox for Matlab.[7] Single nanoparticles with different geometries were embedded in a non-absorbing dielectric medium with a refractive index of 1.33 (water). The sizes and optical properties of the nanorods used in the simulation are listed below. The dielectric function of Au was interpolated from the Johnson-Christy database. For the calculation of the local field-enhancement, a plane wave excitation was always used with polarization vector along x axis, and a propagation vector along - z, see Figure S4. For the calculation of the modified dipole decay rates, dipoles with different eigen-frequencies were placed at logarithmically spaced distances from the particle-surface with higher mesh density close to the nanoparticle surface. For 2D simulations, query points of a 2D mesh on the y-z plane were used for near-field intensity calculations, and at the same points dipoles are placed for the calculation of decay rates. For 1D simulations (as in the rest of the figures), query points were placed only along the center axis of the nanorod, which was on x axis $(y = 0, z = 0)$ logarithmically.

In the MNPBEM toolbox, the decay rates were calculated according to:

$$\frac{\gamma_{\text{nr}}}{\gamma_{\text{r}}^0} = -\frac{1}{2} \Im(\vec{d} \cdot \vec{E}_{\text{ind}}) \tag{6}$$

and

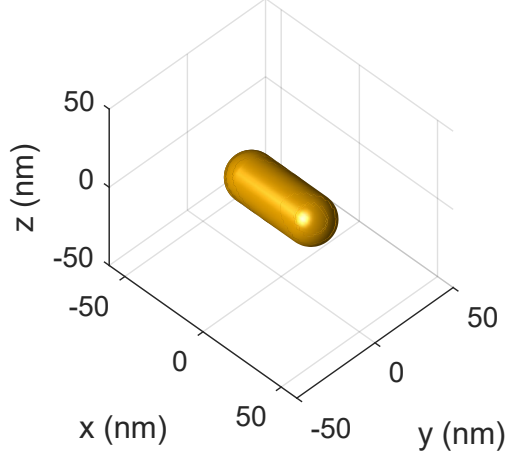$$\frac{\gamma_{\text{r}}}{\gamma_{\text{r}}^0} = |\vec{d} + \vec{d}_{\text{ind}}|^2, \tag{7}$$

Figure S 4: Example of the geometry of the nanorod and coordinate system used in the BEM simulations.

where

γ_{nr} non-radiative decay rate near particle

γ_{r} radiative decay rate near particle

γ_{r}^0 radiative decay rate in free space in the Wigner-Weisskopf approach,

        $\gamma_{\mathrm{r}}^0 = \frac{3}{4} n_{\mathrm{b}} k^3$

$\vec{d}, \vec{d}_{\mathrm{ind}}$ intrinsic and induced dipole transition moment of the

        nanoparticle

n_{b} the refractive index of the embedding medium

k emission wavenumber

$\vec{E}_{\mathrm{ind}}$ the induced electric field at the position of the dipole

For retarded simulations in MNPBEM, the radiative decay rate was computed by integrating the outgoing Poynting vector in the farfield zone over a unit sphere, and the non-radiative decay rate was computed by calculating the Ohmic losses of electromagnetic fields inside the metal. The sum of the radiative decay rate and non-radiative decay rate was the enhanced total decay rate of the dipole γ_{tot}. Here the total decay rate γ_{tot} was calculated to be that of a dipole with an intrinsic quantum yield of unity, i.e. the intrinsic decay of the dipole itself was solely radiative. Therefore in γ_{tot} the non-radiative part was only due to the heat losses in the metal.

Subsequently the orientation averaging of the decay rates was performed outside of the MNPBEM toolbox by averaging the dipoles that are perpendicular and parallel to the particle-surface. Since there are two degrees of freedom for the parallel orientation, the parallel component was multiplied with a factor of 2:

$$\overline{\gamma_{\mathrm{r,nr}}} = \frac{\gamma_{\mathrm{r,nr}}^{\perp} + 2\gamma_{\mathrm{r,nr}}^{\parallel}}{3}. \tag{8}$$

Then modified quantum yield is calculated using:

$$\phi = \frac{\frac{\overline{\gamma_{\mathrm{r}}}}{\gamma_{\mathrm{r}}^{0}}}{\frac{\overline{\gamma_{\mathrm{r}} + \gamma_{\mathrm{nr}}}}{\gamma_{\mathrm{r}}^{0}} + \frac{1-\phi_0}{\phi_0}}, \tag{9}$$

where ϕ_0 is the intrinsic quantum yield of the emitter, which is expressed as:

$$\phi_0 = \frac{\gamma_{\mathrm{r}}^{0}}{\gamma_{\mathrm{r}}^{0} + \gamma_{\mathrm{nr}}^{0} + \gamma_{\mathrm{isc}}^{0}}. \tag{10}$$

The orientation averaged I_{sat} and PCR_{max} are then calculated by:

$$\overline{I_{\mathrm{sat}}} = \frac{\overline{\gamma_{\mathrm{tot}}}}{\sigma_{\mathrm{abs}}} \frac{1}{1 + \gamma_{\mathrm{isc}}/\gamma_{\mathrm{T}}} \tag{11}$$

where $\overline{\gamma_{\mathrm{tot}}}$ is the orientation averaged total decay rate. The orientation averaged PCR_{max} is then given by:

$$\overline{PCR_{\mathrm{max}}} = \eta_{\mathrm{col}} \frac{\sigma_{\mathrm{abs}}}{h\nu} \phi \overline{I_{\mathrm{sat}}}. \tag{12}$$

In order to calculate the wavelength-dependencies in Figure 6, the orientation averaged $\overline{I_{\mathrm{sat}}}$ was divided by the orientation averaged near-field intensity enhancement $|E|^2/|E_0|^2$, which was calculated by $|E|^2/|E_0|^2 = (|E_{\mathrm{x}}|^2/|E_{\mathrm{x0}}|^2 + |E_{\mathrm{y}}|^2/|E_{\mathrm{y0}}|^2 + |E_{\mathrm{z}}|^2/|E_{\mathrm{z0}}|^2)/3$. This was to compensate for the excitation enhancement of the single molecules due to a nearby nanorod. Note that the above orientation averaging applies to fast tumbling molecules which have rotational correlation times shorter than the typical excitation and fluorescence lifetime,

12

and lower enhancement is expected for slowly tumbling molecules due to the fact that only dipoles oriented perpendicularly to the particle-surface will contribute significantly to the enhanced fluorescence.[8]
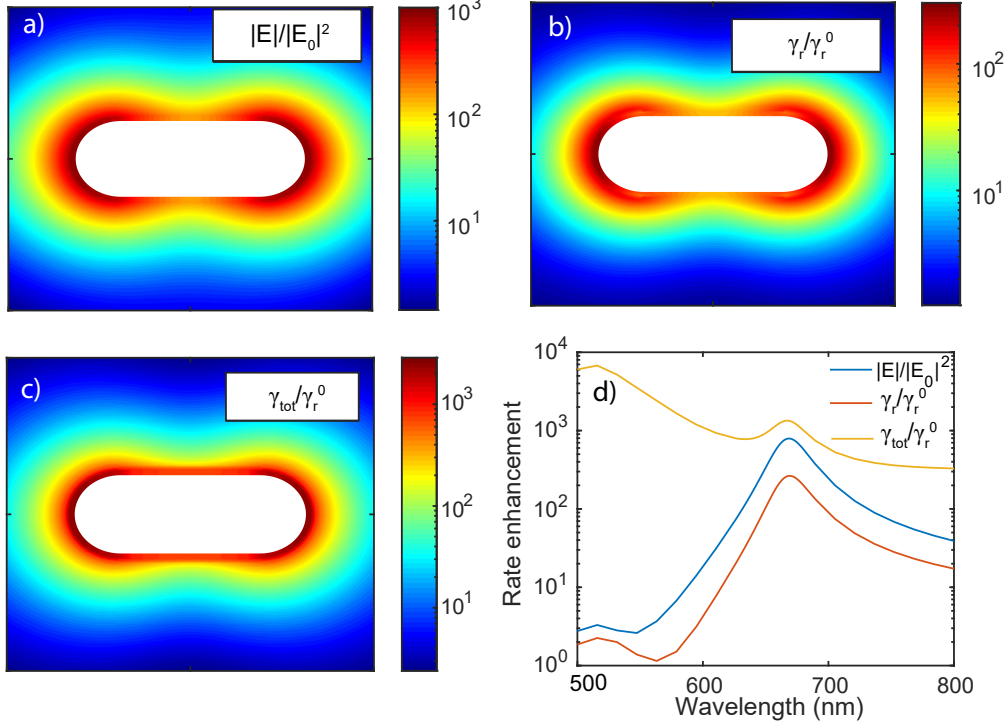

Figure S 5: Numerical calculations of the local field enhancement and rate-enhancements in the vicinity of a single gold nanorod with a size of 63 by 25 nm. (a) Electric near-field intensity normalized to the incident intensity (planewave excitation at 667 nm, polarization along the long axis of the particle). (b)(c) Orientation-averaged radiative and total decay rate modifications as a function of fluorophore position. Fluorophores are assumed to be single-wvaelength dipole emitters with quantum yield of unity at 664 nm. (d) Modification of the near-field intensity (plotted a function of excitation wavelength) and the (non-)radiative rates (plotted as a function of fluorophore emission wavelength). The emitter was placed at 2 nm from the nanorod's tip.

Figure S5(a) shows the numerically calculated near field intensity around a gold nanorod of 63×25 nm^2, evaluated at on resonance with the longitudinal plasmon at 667 nm. An enhanced intensity around the two tips of the gold nanorod of about $\frac{|E|^2}{|E_0|^2} \simeq 1000$ is found, where E is the local field and E_0 the incident field. In Figure S5(b) and (c) we show the calculated radiative and total decay rates γ_r and γ_{tot} in units of the free-space rates. Both excitation and emission rate modifications are also strongly confined to the particle surface,

and decay rapidly away from the surface on length-scales of $\sim 1-5$ nm. In Figure S5(d) we show the wavelength-dependence of the enhancements. We observe a strong SPR-dependent enhancement, and in all cases a maximum enhancement is reached when excitation or dipole emission overlap with the longitudinal plasmon resonance of the nanorod. The non-radiative decay rate is also strongly modified off-resonance due to energy transfer to interband electrons in gold.[9]

The photophysical parameters used to simulate the saturation dynamics of a free-space ATTO647N is shown in Table 2. These parameters were then used to reproduce the experimental saturation curve measured with single-molecule fluorescence microscopy, and used as the free-space reference of plasmon-enhanced simulations.

Table 2: Photophysical parameters used to simulate the free-space PCR of a single ATTO647N[10]

Parameters	Values (unit)
σ_{abs}	$5.7 \times 10^{-20}\text{m}^2$
η_{col}	0.02
$h(\text{Plank's constant})$	$6.6 \times 10^{-34}\text{J s}$
$c(\text{speed of light})$	$3.0 \times 10^8 \text{m s}^{-1}$
τ_{tot}^0	3.5ns
γ_{tot}^0	$2.9 \times 10^8 \text{s}^{-1}$
γ_{r}^0	$1.8 \times 10^8 \text{s}^{-1}$
$\gamma_{\text{isc}}/\gamma_{\text{T}}$	300
ϕ_0	0.65

In Table 3 we show the list of gold nanorod sizes used in the simulation of Figure 2 and 6, which are gold nanorods with fixed widths but varying lengths and SPR wavelengths.

In Table 4 we show the list of gold nanorod sizes used in the simulation of Figure 7, which are gold nanorods with fixed SPR but varying volumes.

In Figure S6(b) we show the computed PCR_{max}, where strongest PCR_{max} is found for nanorods with diameters < 20 nm, and decreases by a factor of up to 10 when the diameter increases to $60\,\text{nm}$. The origin of this is comparable with the inverse mode volume dependence of the radiative rate in the context of Purcell enhancement.[9] In Figure S6(c) we show the computed I_{sat} (plotted as the far-field laser power density), where we find that

Table 3: Simulated nanorod dimensions with fixed widths, varying in lengths and SPR wavelengths as in Figure 2 and 6

Dimensions (nm^2)	SPR (nm)
29 × 25	544
33 × 25	554
38 × 25	570
42 × 25	583
46 × 25	597
48 × 25	604
50 × 25	612
54 × 25	628
58 × 25	645
61 × 25	658
63 × 25	667
67 × 25	685
69 × 25	695
75 × 25	724

Table 4: Simulated nanorod dimensions with fixed SPR but varying volumes as in Figure 7

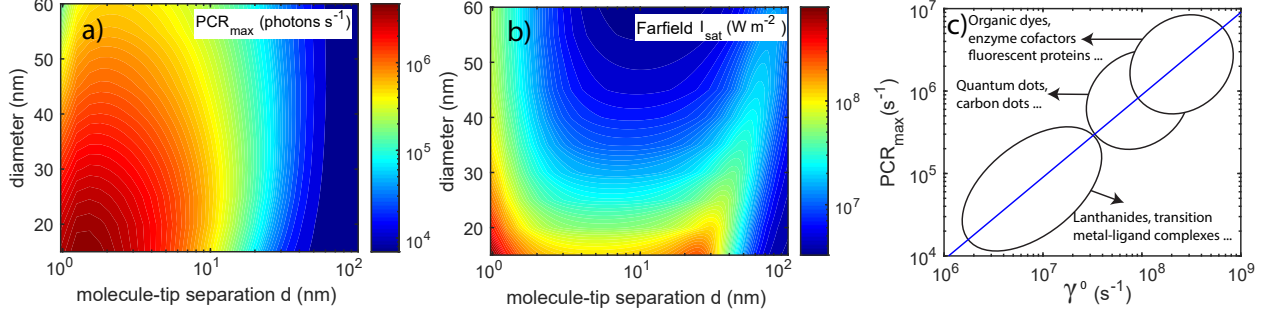| Dimensions (nm^2)	SPR (nm)
40 × 15	667
52 × 20	666
63 × 25	666
73 × 30	667
82 × 35	667
90 × 40	668
97 × 45	668
109 × 55	668
114 × 60	667

Figure S 6: Simulation results of (a) PCR_{max} and (b) I_{sat} as a function of molecule-tip separation distance d (nm) and nanorods diameters. Simulation is performed with a fixed gold nanorod SPR wavelength of 664 nm by varying the diameters and accordingly adjusting the heights, $\lambda_{\mathrm{exc}} = 637$nm, $\lambda_{\mathrm{em}} = 664$nm, $\phi_0 = 0.65$, and the fluorophore as an emitting dipole is place at along the center axis of the nanorod starting at $d = 0.8$nm from the tip. (c) Theoretical evaluation of plasmon-enhanced PCR_{max} as a function of intrinsic radiative rates of different types of fluorophores. Simulation is performed with a fixed gold nanorod dimension of 63×25 nm, $\lambda_{\mathrm{exc}} = 637$nm, $\lambda_{\mathrm{em}} = 664$nm, $\phi_0 = 0.65$, and the fluorophore as an emitting dipole is placed at $d = 4$ nm away from the tip along the center axis of the nanorod. See supporting information for full simulation parameters.

although small particles provide high PCR_{max}, they are also more difficult to saturate and require power densities up to 10^9 W m^{-2}. These power densities are not easily attainable with wide-field microscopy but feasible with a focused laser, e.g. in a confocal microscope. We thus find a practical size of gold nanorods of $20 - 30$nm for PCR_{max} enhancement . We show in Figure S6(c) a chart of the plasmon-enhanced PCR_{max} as a function of γ_{r}^0. A linear trend of PCR_{max} is found in γ_{r}^0 as expected. It is interesing to note that the intrinsic quantum yield of the emitter does not dominate the process because the nanoparticle-molecule complex emits with an efficiency close to the radiating efficiency of the plasmons, which is nearly independent of the intrinsic efficiency of the molecule. [9]

References

1. Chen, H.; Meisburger, S. P.; Pabit, S. A.; Sutton, J. L.; Webb, W. W.; Pollack, L. Ionic strength-dependent persistence lengths of single-stranded RNA and DNA. *Proceedings of the National Academy of Sciences* **2012**, *109*, 799–804.

2. Manning, G. S. The response of DNA length and twist to changes in ionic strength. *Biopolymers* **2015**, *103*, 223–226.

3. El Arawi, D.; Cardoso Dos Santos, M.; VÃ'zy, C.; Jaffiol, R. Incidence angle calibration for prismless total internal reflection fluorescence microscopy. *Optics Letters* **2019**, *44*, 1710.

4. Schnitzbauer, J.; Strauss, M. T.; Schlichthaerle, T.; Schueder, F.; Jungmann, R. Super-resolution microscopy with DNA-PAINT. *Nature Protocols* **2017**, *12*, 1198–1228.

5. Visscher K.,; Brakenhoff G. J.,; Visser T. D., Fluorescence saturation in confocal microscopy. *Journal of Microscopy* **2011**, *175*, 162–165.

6. Moerner, W. E.; Fromm, D. P. Methods of single-molecule fluorescence spectroscopy and microscopy. *Review of Scientific Instruments* **2003**, *74*, 3597–3619.

7. Hohenester, U.; Trügler, A. MNPBEM A Matlab toolbox for the simulation of plasmonic nanoparticles. *Computer Physics Communications* **2012**, *183*, 370–381.

8. Wang, Y.; Zijlstra, P. Plasmon-Enhanced Single-Molecule Enzymology. *ACS Photonics* **2018**, *5*, 3073–3081.

9. Mertens, H.; Koenderink, A. F.; Polman, A. Plasmon-enhanced luminescence near noble-metal nanospheres: Comparison of exact theory and an improved Gersten and Nitzan model. *Physical Review B* **2007**, *76*.

10. Oracz, J.; Westphal, V.; Radzewicz, C.; Sahl, S. J.; Hell, S. W. Photobleaching in STED nanoscopy and its dependence on the photon flux applied for reversible silencing of the fluorophore. *Scientific Reports* **2017**, *7*, 11354.